Weyl points and spin-orbit coupling in copper-substituted lead phosphate apatite

Martin Braß,[1] Liang Si,[2] and Karsten Held[1]
[1]*Institute of Solid State Physics, TU Wien, 1040 Vienna, Austria*
[2]*School of Physics, Northwest University, Xi'an 710127, China*

(Received 12 October 2023; revised 7 December 2023; accepted 5 January 2024; published 2 February 2024)

We study the impact of spin-orbit coupling on the topological band properties of copper-substituted lead phosphate apatite using a combination of group-theoretical analysis and full-relativistic density-functional theory calculations. We characterize Weyl points at time-reversal invariant momenta and find that a band inversion due to spin-orbit coupling leads to additional Weyl points close to the Fermi edge at general momenta. To determine the position of the altogether 66 Weyl points in the Brillouin zone, we develop an algorithm that follows a Berry-curvature-derived vector field to its monopole: the Weyl point. The emerging surface Fermi arcs and their spin polarization reveal avoided crossings and a Fermi loop detached from the Weyl points.

DOI: 10.1103/PhysRevB.109.085103

I. INTRODUCTION

Recent pronouncements of room temperature superconductivity [1–3] have put copper substituted lead apatite $Pb_9Cu(PO_4)_6O$ into the focus of solid state research. Subsequent work has shown that—without further doping—$Pb_{10-x}Cu_x(PO_4)_6O$ is a Mott or charge transfer insulator for all x [4–14] and that the observed conductivity jumps likely originate from residual Cu_2S [13,15,16].

Even without superconductivity, $Pb_9Cu(PO_4)_6O$ is interesting in its own right. Its band structure in density functional theory (DFT) [4,17–19] exhibits two almost flat bands which cross the Fermi edge and are formed by the Cu d_{xz}/d_{yz} orbitals. The symmetry properties of the compound imply that these bands contain Weyl points [20,21] which may impact thermal as well as electromagnetic transport properties and give rise to topologically protected surface states. Despite its importance and topicality, Weyl points in $Pb_9Cu(PO_4)_6O$ also known as LK-99 have not been deeply investigated hitherto.

Here, we construct a tight-binding model from DFT calculations of the electronic band structure in Sec. II. We study the topological properties of this compound with a group-theoretical analysis to characterize all symmetry protected Weyl points at time-reversal invariant momenta in the presence and absence of spin-orbit coupling (SOC) in Sec. III. In combination with the band-structure calculations this uncovers the emergence of additional Weyl points at general momenta due to the influence of SOC. To detect these Weyl points automatically we present an algorithm in Sec. IV. With SOC, there are additional Weyl points close to the Fermi surface resulting in surface Fermi arcs as described in Sec. V.

Before starting, let us put some caveats here. (i) We consider the lowest energy structure (for a single unit cell) of $Pb_9Cu(PO_4)_6O$, as shown in Fig. 1(a). This has a *P3* (no. 143) space group, but other structures (other orientations of the "extra" or channel O and of the Cu) are only ∼6 meV per unit cell different in energy [4]. This means that observing a single crystal instead of a disordered compound requires temperatures well below 6 meV (70 K) or under pressure >73 GPa according to DFT calculations [22].

(ii) Since $Pb_{10-x}Cu_x(PO_4)_6O$ is insulating, a slight electron or hole doping is required to obtain the Weyl points studied here on the DFT level. Such an electron or hole doping is not possible by changing x as Cu and Pb are both 2+. Instead O excess or deficiency, substituting P by S or other means that change the valence on the Cu sites is needed. With such a doping, a quasiparticle peak will emerge at the Fermi level which is a renormalized (more narrow) version of the electronic structure analyzed in the present paper.

II. BAND STRUCTURE FROM FIRST PRINCIPLE CALCULATIONS

For our analysis of topological properties we start from the relaxed crystal structure with *P3* (no. 143) space group displayed in Fig. 1(a). Here, Cu and the additional O occupy positions farthest away from each other [4]. It has been shown that the electronic structure close to the Fermi energy can be effectively described by two flat bands corresponding to Cu d_{xz}/d_{yz} orbitals [4,17–19].

To construct a tight-binding model that captures the topology of this two-band system, we perform a self-consistent DFT calculation and Wannier projection onto the Cu d_{xz}/d_{yz} orbitals using the full potential local orbital (FPLO) code [23]. We use a dense $(11 \times 11 \times 15)$ k mesh and the Perdew-Wang exchange-correlation potential [24] for a scalar-relativistic and a fully relativistic DFT calculation, i.e., a DFT calculation without and with SOC.

The obtained band structure is shown in Fig. 1(c) and agrees well with previous results [4,9,13,17,18]. While band crossings can be seen only at the high symmetry points Γ and A in the case without SOC (blue, dashed curve), the case with SOC (red) involves crossings at every time-reversal invariant momentum. We will discuss their topological properties in the following section. At the points K and H the bands are

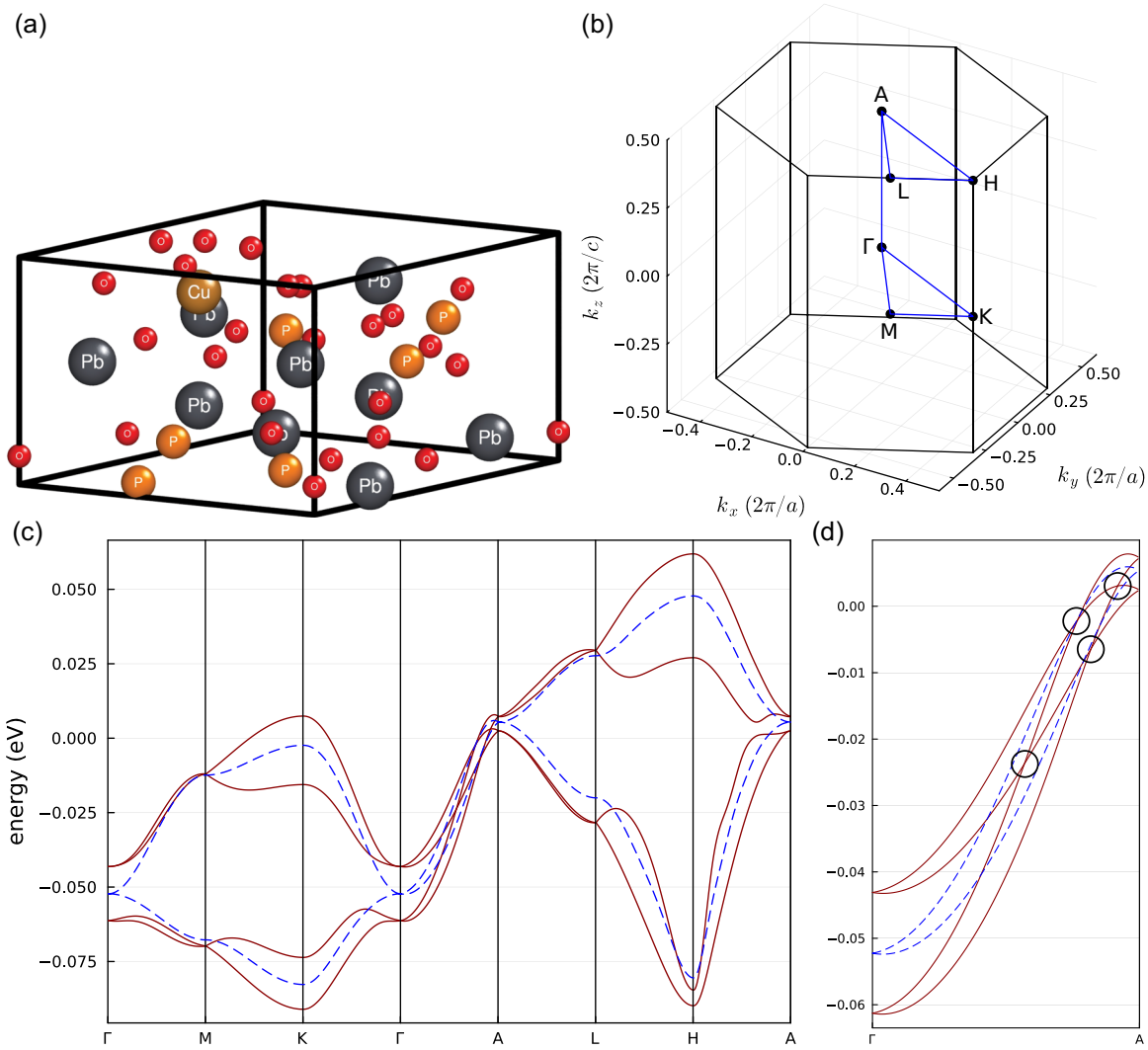

FIG. 1. (a) Crystal structure of $Pb_9Cu(PO_4)_6O$. (b) Points of high symmetry in the Brillouin zone: $\Gamma = (0, 0, 0)$, $M = (1/4, -\sqrt{3}/4, 0)$, $K = (1/2, -1/\sqrt{12}, 0)$, $A = (0, 0, 1/2)$, $L = (1/4, -\sqrt{3}/4, 1/2)$, and $H = (1/2, -1/\sqrt{12}, 1/2)$. The blue line is the path along which the band structure is plotted in the following. (c) Band structure close to the Fermi level. The blue, dashed lines depict the Cu d_{xz}/d_{yz} bands obtained by a scalar-relativistic DFT calculation without SOC. Band crossings are enforced by symmetry at Γ and A. The solid red lines are the Cu $d^{j=5/2}_{m=\pm 3/2,\pm 1/2}$ bands obtained by a full-relativistic DFT calculation. TR symmetry enforces Kramers' degeneracy at all TRIM. (d) Zoom-in along the $\Gamma - A$ direction. Band inversion due to SOC yields additional band crossings close to the Fermi surface (marked by circles).

nondegenerate due to the missing inversion symmetry and the corresponding eigenstates are $d_{xz} \pm i d_{yz}$ [25,26].

III. SYMMETRY AND SPIN-ORBIT COUPLING

The presence of time-reversal (TR) symmetry enforces spin-degenerate bands to cross at time-reversal invariant momenta (TRIM) if these host complex valued irreducible representations of their corresponding little groups. The space-group symmetry of the crystal system is *P3* (no. 143) and therefore the only point symmetry is a C_3 rotation around the z axis. Consequently, the little groups at any k point are Abelian and have one-dimensional irreducible representations [27].

The little group of the TRIM Γ and A is C_3 and the real valued d_{xz}/d_{yz} orbitals can be decomposed into complex valued irreducible representations given by the spherical harmonics $Y_2^{\pm 1}$. Therefore, LK99 features symmetry protected band crossings at the TRIM Γ and A.

Close to a band crossing at momentum $\mathbf{k}_0$ the Bloch Hamiltonian can be expressed as

$$H_{\mathbf{k}} = \mathbf{h}(\mathbf{q}) \cdot \boldsymbol{\sigma} + E(\mathbf{k}_0), \tag{1}$$

where $\mathbf{h}(\mathbf{q})$ is a smooth function of momentum $\mathbf{q} = \mathbf{k} - \mathbf{k}_0$, $\boldsymbol{\sigma}$ denotes the Pauli matrices, and $E(\mathbf{k}_0)$ is the energy at the crossing. The associated Chern number can be calculated as [28]

$$C = \frac{1}{4\pi} \int_{S^2} \left(\frac{\partial \hat{\mathbf{h}}(\mathbf{q})}{\partial q^i} \times \frac{\partial \hat{\mathbf{h}}(\mathbf{q})}{\partial q^j} \right) \cdot \hat{\mathbf{h}} \, \mathrm{d}q^i \wedge \mathrm{d}q^j. \tag{2}$$

Here and in the following, sum convention is implied, $\hat{\mathbf{h}}(\mathbf{q}) = \frac{\mathbf{h}(\mathbf{q})}{\|\mathbf{h}(\mathbf{q})\|}$, and S^2 denotes a sphere surrounding the Weyl point. In the language of differential topology, this Chern number is

just the degree of the smooth map $\hat{\mathbf{h}} : S^2 \to S^2$, which we can determine via [29]

$$C \equiv \deg(\hat{\mathbf{h}}) = \sum_{\mathbf{q}\in\hat{\mathbf{h}}^{-1}(\boldsymbol{\eta})} \operatorname{sgn}[\det(\mathrm{d}\hat{\mathbf{h}}|_{\mathbf{q}})], \tag{3}$$

where $\mathrm{d}\hat{\mathbf{h}}|_{\mathbf{q}}$ is the differential (i.e., Jacobian) of $\hat{\mathbf{h}}$ evaluated at a momentum $\mathbf{q}$ from the preimage $\hat{\mathbf{h}}^{-1}(\boldsymbol{\eta})$ of any regular value $\boldsymbol{\eta}$ of $\hat{\mathbf{h}}$.$\boldsymbol{\eta}$ is called a regular value of $\hat{\mathbf{h}}$ if its preimage $\hat{\mathbf{h}}^{-1}(\boldsymbol{\eta}) = \{\mathbf{q}_1, \ldots, \mathbf{q}_r\}$ consists of points at which the differential of $\hat{\mathbf{h}}$ has full rank. If s denotes the number of points in $\hat{\mathbf{h}}^{-1}(\boldsymbol{\eta})$ at which $\hat{\mathbf{h}}$ changes orientation, then the degree of $\hat{\mathbf{h}}$ equals $r - s$.

A band crossing at $\mathbf{k}_0$ is a Weyl point if and only if the Chern number and so the degree of $\hat{\mathbf{h}}$ is nonzero. When moving away from the crossing, the bands generically have to split in every direction due to the low symmetry of our system. This favors the crossings to be Weyl points and indeed a numerical calculation confirms this for all band crossings we found. Therefore, we will assume for the following theoretical considerations that the band crossings have non vanishing Chern number and are hence Weyl points.

Time-reversal and C_3 symmetry almost completely determine the degree of $\hat{\mathbf{h}}$ up to its sign as we explain in Appendix A. The basic idea is to first infer how $\hat{\mathbf{h}}$ transforms under symmetry operations from the representation of the crossing bands. Then this can be used to determine the number of summation points $\mathbf{q}$ in Eq. (3) from the preimage $\hat{\mathbf{h}}^{-1}(\boldsymbol{\eta})$ of a regular value $\boldsymbol{\eta}$ and also if the Jacobian determinant changes sign at these points. The overall sign of C, however, is not fixed by symmetry alone. Thus this information obtained from symmetry can be used to determine the absolute value of the Chern number from Eq. (3). To put it differently, the symmetry properties of $\hat{\mathbf{h}}$ can predict how many momenta $\mathbf{q}$ are mapped via $\hat{\mathbf{h}}$ onto the same value. Counting these and considering the change in orientation of $\hat{\mathbf{h}}$ gives us the Chern number of the Weyl point.

Let us start with the case without SOC. In Appendix A we find that, for the TRIM Γ and A the representations of the Cu d_{xz}/d_{yz} orbitals ensure that the x and y components of $\hat{\mathbf{h}}$ are even and the z component is odd under time reversal. If we pick a regular value $\boldsymbol{\eta}$ with $\eta_z = 0$, then its preimage contains at least two points which are time reversal symmetric partners. At these points the Jacobian determinant must have the same sign, since TR reverses orientation in the Brillouin zone, but also reverses $\hat{h}_z$. Hence the sum in Eq. (3) runs over at least these two points.

Under the threefold rotation around the z axis $\hat{\mathbf{h}}$ transforms as a three-dimensional (3D) vector for the given representation of Cu d_{xz}/d_{yz} bands. Hence this rotation changes $\hat{\mathbf{h}}$ and therefore does not add further points to the preimage of $\boldsymbol{\eta}$. Consequently, the sum in Eq. (3) generically runs over the two time reversal partners only and thus $\hat{\mathbf{h}}$ wraps around the sphere twice, such that Chern numbers at Γ and A generically have absolute values equal to two [21,30]. To determine the sign, we calculate Eq. (2) numerically and obtain Chern numbers equal to -2 at Γ and $+2$ at A, respectively.

The situation changes if we take SOC into account. Then each of the two bands splits, yielding four bands in total as shown in Fig. 1(c), where we present the band structure of a full-relativistic DFT calculation (red curve). These bands belong to those copper $3d_{5/2}$ orbitals which have $j_z = \pm 1/2$ and $j_z = \pm 3/2$. However, now having a spin-full representation of the corresponding double group, the TR operator squares to -1 thereby enforcing Kramers' degeneracies of the bands at every TRIM [31]. Hence there are further Weyl points at M and L additional to those at Γ and A. Furthermore, this is valid for both pairs of bands, which implies that every TRIM holds two Weyl points at different energies. This is especially interesting for A where Weyl points are very close to the Fermi energy $\epsilon_F = 0$ as can be seen in Fig. 1(c).

To determine the Chern numbers at TRIM, we proceed as before and use Eq. (3) together with symmetry arguments. As discussed in Appendix A, $\hat{\mathbf{h}}$ is odd under TR. Therefore, TR enforces the band crossings at TRIM, but does not lead to additional points in the preimage of a regular value η. At M and L the corresponding little groups are the trivial group, i.e., only the neutral element leaves these points invariant [32]. Therefore, symmetry does not enforce different momenta $\mathbf{q}$ to be mapped onto the same regular value η. Hence its preimage generically contains a single point and thus the Chern numbers at M and L must have an absolute value equal to one.

At Γ and A the Chern numbers depend on the character of the bands. Due to the presence of time-reversal symmetry the degenerate bands have either $j_z = \pm\frac{1}{2}$ or $j_z = \pm\frac{3}{2}$. From this we can deduce how the orbitals and hence also $\hat{\mathbf{h}}$ in Eq. (1) transform under a threefold rotation around the z axis, as we show in Appendix A. In the case of the $j_z = \pm\frac{3}{2}$ bands, $\mathbf{h}$ and consequently also $\hat{\mathbf{h}}$ remain invariant. Thus there are always three points $\mathbf{q}$ on the sphere related by the threefold rotation which are mapped onto the same value under $\hat{\mathbf{h}}$. At these points the change of orientation is the same, since rotations preserve orientation. Consequently, Eq. (3) implies Chern numbers equal to plus or minus three for the $j_z = \pm\frac{3}{2}$ bands.

In the case of the $j_z = \pm\frac{1}{2}$ bands, $\hat{\mathbf{h}}$ transforms as a 3D vector, as we again detail in Appendix A. This implies that a rotation changes the value of $\hat{\mathbf{h}}$, and so for any value there is generically only a single point mapped onto this value. Consequently, the sum in Eq. (3) runs over a single point and therefore the absolute value of the corresponding Chern number is one.

However, only a direct calculation can determine the characters of the bands. From our full relativistic DFT calculation we find that at Γ the upper band is of $\pm\frac{3}{2}$ character and the lower one $\pm\frac{1}{2}$. Hence we obtain Chern numbers equal to $C = +3$ and $C = -1$, respectively. At A the situation is reversed yielding $C = +1$ for the upper and $C = -3$ for the lower band.

At M we get a Chern number $C = -1$ and $C = +1$ at L for the upper bands. For the lower ones they are $C = +1$ at both M and L. Hence, if we sum up the Chern numbers of the upper band, we arrive at a total of $+4$ and $+2$ for the lower band (note that L and M are threefold, due to the C_3 axis). Since the Nielsen-Ninomiya theorem enforces a total of zero Chern numbers [33,34], there must be additional Weyl points not protected by symmetry.

In Fig. 1(c) we can see band crossings at the TRIM, but also at the line from Γ to A in Fig. 1(d). The latter crossings are close to the Fermi energy $\epsilon_F = 0$ and also somewhat below. Due to TR invariance the same crossings must appear at the

corresponding negative momenta on the line from Γ to $-A$. We calculate the Chern numbers of these crossing points. For the lowest band there is one Weyl point with $C = -1$ and its time-reversal partner with the same Chern number. Thus, for the lowest band, the total of Chern numbers vanishes. For the remaining bands, we do the same calculation, but find that the total does not equal zero. Consequently there must be additional Weyl points at general momenta that are not on the high symmetry k path shown in Fig. 1(c). We have to find them manually.

IV. ALGORITHM TO DETECT WEYL POINTS

Finding Weyl points whose positions are not determined by symmetry arguments can be a peculiar task. Typical approaches divide the Brillouin zone into multiple parallelepipeds, integrate the Berry curvature over their surfaces, and refine the enclosed volume if it has a nonvanishing Chern number [35]. Alternatively, there is a method based on Wilson loops [36] and on a direct search for local minima in the band gap [37]. Here, we propose a different approach that can be used complementary to the others. It is based on the fact that Weyl points act as sources and sinks of Berry curvature [38]:

$$\Omega^n_{ij} = -\mathrm{Im}\left[\sum_{m\neq n} \frac{\langle\psi^n_k|\partial_{k^i}H(k)|\psi^m_k\rangle\langle\psi^m_k|\partial_{k^j}H(k)|\psi^n_k\rangle}{[E_m(k)-E_n(k)]^2}\right]. \quad (4)$$

Here, ψ^n_k denotes an eigenstate of the Bloch Hamiltonian $H(k)$ with band index n, momentum k, and energy $E_n(k)$.

More precisely, for a fixed band index n we can understand the Berry curvature Eq. (4) as a differential two-form $\Omega^n := \Omega^n_{ij}\mathrm{d}k^i \wedge \mathrm{d}k^j$ on the Brillouin zone without the Weyl points. In 3D we can use the Hodge-$\star$ [39] to identify Ω^n with the one-form $\star\Omega^n = \Omega^n_{ij}\epsilon_{ijl}\mathrm{d}k^l =: X_l\mathrm{d}k^l$ and use the canonical isomorphism of tangent and cotangent space to finally identify it with a vector field $X = X^i\partial_{k^i}$.

To find a Weyl point, we pick a starting point k in the Brillouin zone and search for an integral curve $\gamma(t)$ of X with $\gamma(0) = k$. That is, we solve the ordinary differential equation

$$\frac{\mathrm{d}\gamma}{\mathrm{d}t} = X(\gamma(t)). \quad (5)$$

If the solution converges to a point in finite time, we have found a band crossing, which acts as a sink of the vector field X. Otherwise, we may get a closed curve, and then disregard it and pick another starting point.

To find all points we apply this procedure to multiple starting vectors distributed over the whole Brillouin zone. This is trivially parallelizable. In order to also find sources instead of sinks, we apply the procedure to $-X$. For the numerical solution of Eq. (5) we apply the implicit Euler method with adaptive step size [40]. Therefore, Eq. (4) needs to be evaluated in every step. The partial derivative of the Hamiltonian with respect to momentum can be done analytically for a tight-binding or Wannier Hamiltonian. The eigenvalues and eigenvectors of $H(\mathbf{k})$ are found with standard linear algebra routines [41].

Thus we can find the remaining Weyl points. For the upper pair of bands, we detect 32 and 34 for the lower pair of bands (including those described earlier), which are shown in Fig. 2.

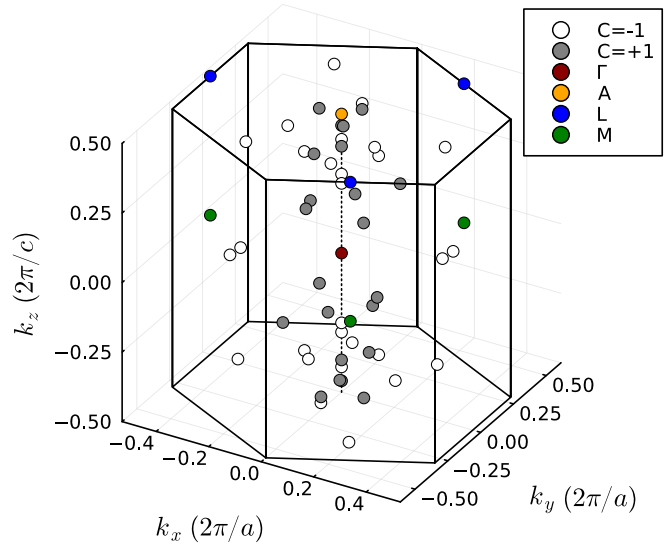

FIG. 2. Weyl points in the Brillouin zone. The color code denotes the different Chern numbers C. At TRIM, the Chern numbers are different for the $j_z = \pm\frac{1}{2}$ and $j_z = \pm\frac{3}{2}$ bands (see text).

To confirm the validity of the algorithm, we calculate the Chern numbers of the points via an integration of Eq. (4) over a small sphere surrounding a point. This confirmed that we did not get false positives. We also sum up all Chern numbers yielding zero as it must be. Our algorithm detected all Weyl points at TRIM and also those at general momenta without any guidance. Hence it is suitable for the automatic detection of Weyl points.

Note that this algorithm is similar to the method used by Weng *et al.* [42] in the sense that Weyl points are identified by their property being sinks and sources of Berry curvature. However, solving the differential equation (5) has two advantages. First, there is no need for manual inspection and hence our algorithm allows for automatization, which might be suitable for high-throughput calculations. Second, solving an ordinary differential equation reduces the number of evaluations of the Berry curvature as compared to sampling it on the whole (irreducible) Brillouin zone. Using an adaptive step-size algorithm ensures that the Berry curvature is sampled more densely only in the vicinity of a Weyl point. This becomes important in systems where variations in Berry curvature are very localized or where many bands need to be included in the Wannier Hamiltonian such that evaluation of Ω is computationally expensive.

V. SURFACE STATES

Due to the bulk-boundary correspondence, the presence of Weyl points implies the existence of Fermi arcs, i.e., states of constant energy that are localized on a surface of the crystal. They appear if the corresponding reciprocal surface in k space contains projections of Weyl points with opposite chiralities that do not fall on the same point [43]. Fermi arcs can be determined by angle resolved photoemission spectroscopy (ARPES) [44,45] and can be calculated via the surface

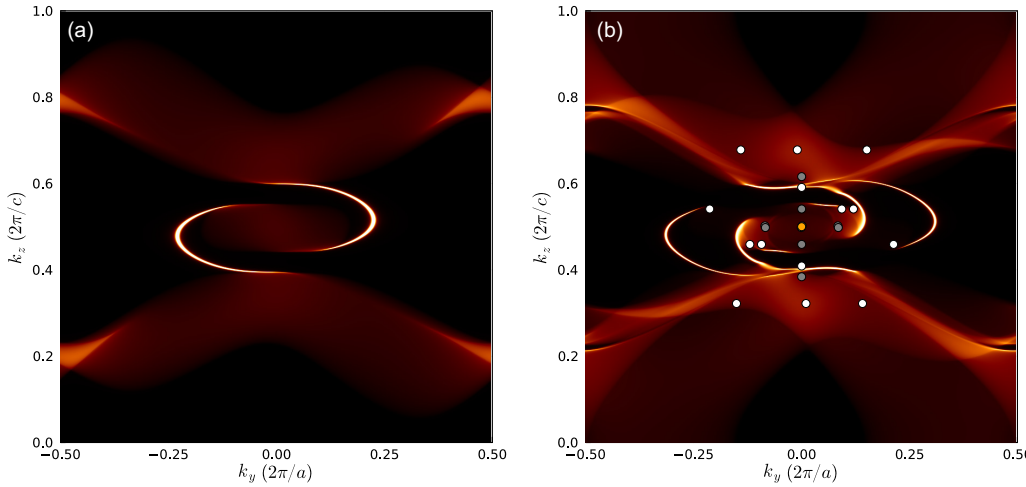

FIG. 3. Surface spectral density $A(k_y, k_z, \omega = \epsilon_F)$ calculated from Eq. (6) for a semi-infinite crystal terminated at the $x = 0$ surface. (a) Without SOC there are two Fermi arcs connecting those parts of the Fermi surface that surround the projections of Weyl points at Γ and A with Chern numbers equal to -2 and $+2$, respectively. (b) SOC leads to the appearance of further Fermi arcs. The Weyl points are color coded as in Fig. 2, but we show only those close to the Fermi level. Two Weyl points with $C = +1$ are projected onto the same point as A (orange). To the left and right of A, Weyl points (gray) with $C = +1$ are projected onto the same point as well.

spectral density of a semi-infinite crystal [46]

$$A(k_y, k_z, \omega) = -\mathrm{Im}\left[\mathrm{Tr}\left(\frac{1}{\omega + i0^+ - H(k_y, k_z)}\right)\right]. \quad (6)$$

Here we choose to terminate the crystal at the $x = 0$ surface. Hence $H(k_y, k_z)$ denotes the Fourier-transformed tight-binding Hamiltonian where hopping is retained in the positive x direction only. The trace Tr runs over all states localized at the surface. For numerical calculations we truncate the system after 1344 layers and choose the positive infinitesimal to be $0^+ = 10^{-4}$.

Figure 3(a) shows the projected Fermi surface and Fermi arcs for our calculation without SOC. The Fermi surface consists of three disconnected parts. The central one encloses the projection of the Weyl point at A. Due to periodicity of the Brillouin zone, the other two parts sandwich the projection of the Weyl point at Γ. Since the Chern number of the Weyl point at A in the center ($k_z = 1/2$) is $+2$ and that of Γ at the top or bottom ($k_z = 0, 1$) is -2, there are two arcs connecting the different parts of the Fermi surface. Note, the arcs do not exactly terminate at A and Γ because these momenta are not precisely at the Fermi energy.

If we consider the full-relativistic calculation, that includes SOC, the situation becomes more complex due to the presence of multiple Weyl points as shown in Fig. 3(b). Due to SOC the bands are wider and the projected Fermi surface merges in the k_z direction, such that compared to the case without SOC we only have two disconnected parts: a central one and the merged top/bottom part. Outside those parts we observe two isolated Weyl points (white circles) which are essentially at the Fermi level. Therefore, from each of them one arc emerges and connects the Weyl points to the top/bottom part of the Fermi surface.

The central part encloses multiple projections of Weyl points which are a bit farther away from the Fermi energy. Hence we observe two additional arcs that do not start at a Weyl point, but connect the central part with the top/bottom part of the Fermi surface. Tangential [47] at the central part we can see two further arcs, which are small and almost horizontal. They connect Weyl points of opposite chirality (white and gray) that are both projected onto the same component of the Fermi surface. For all these arcs we confirm their topological nature by calculating the surface-projected band structure along loops surrounding a Weyl point and observe topological edge states that connect the upper bulk-projected band with the lower one [45]. Hence, compared to Fig. 3(a), SOC enriches the Fermi surface with additional topologically protected states.

Furthermore, SOC can lead to interesting patterns in the spin polarization or spin texture of a surface. This can be measured with spin-resolved ARPES [48,49]. In the following, we study the spin polarization of the surface states at different Fermi levels. For the same semi-infinite crystal as above, we can calculate the surface spin polarization via

$$\mathbf{P}(k_y, k_z, \omega) = -\mathrm{Im}\left[\mathrm{Tr}\left(\frac{\mathbf{S}}{\omega + i0^+ - H(k_y, k_z)}\right)\right], \quad (7)$$

where $\mathbf{S}$ denotes the spin operator and the trace is again taken over all states localized at the surface. The results are shown in Fig. 4.

At a Fermi energy equal to -57.0 meV in Fig. 4(a), we see two U-shaped surface arcs, where the spin projection onto the yz plane points into different directions for the arcs. If the Fermi energy is increased to -56.5 meV [4(b)] the arcs touch and the spin projection winds around the touching point. Upon further increase in the Fermi energy [4(c), 4(d)] we observe avoided crossings which turn the two U-shaped arcs into two horizontal arcs and a detached loop in the center. The spin projection winds around this loop and near the avoided crossings we can observe changes in polarization as expected in such a situation. This is the same for the projection of $\mathbf{P}$ onto the xz plane as shown in the Appendixes. Hence all spin components of the surface states wind around the central loop.

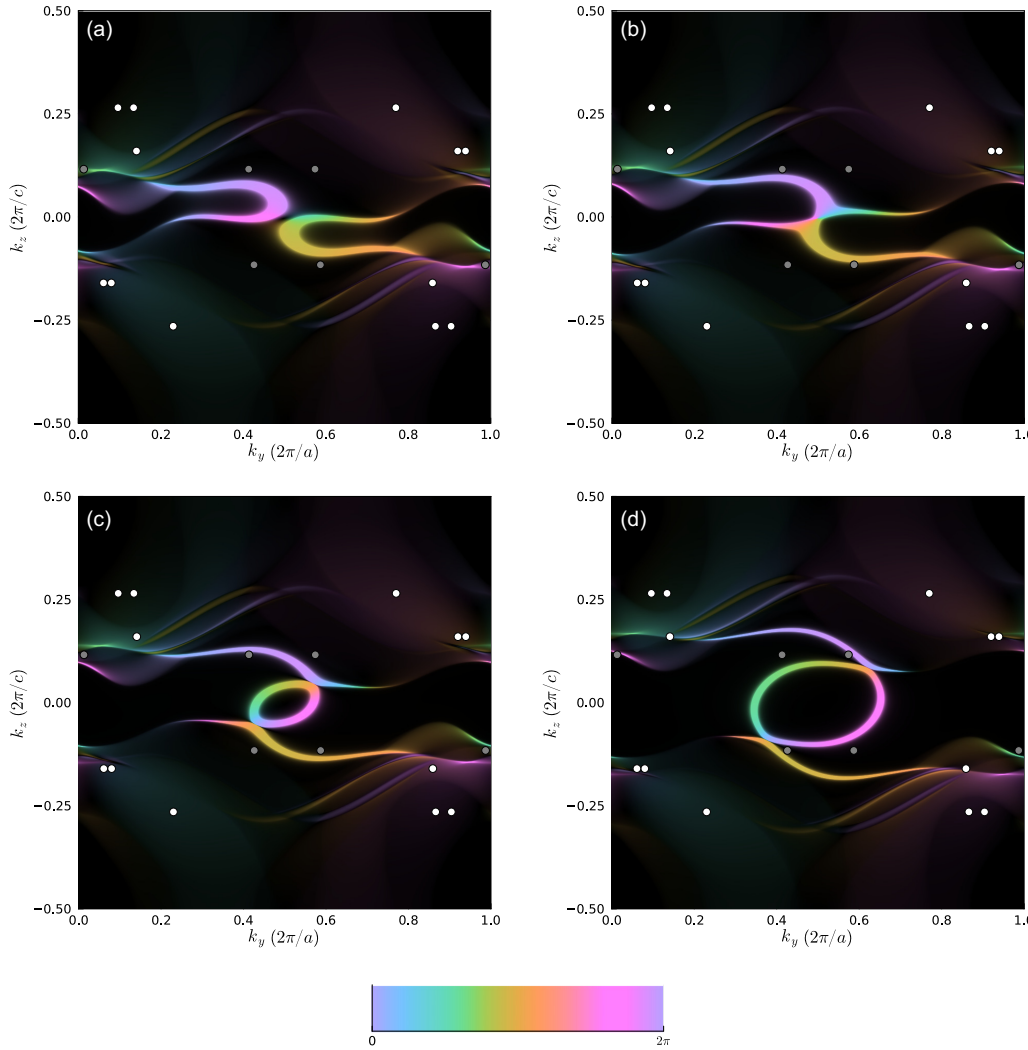

FIG. 4. Surface spectral spin density $\mathbf{P}(k_y, k_z, \omega = \epsilon_F)$ calculated from Eq. (7) for a semi-infinite crystal terminated at the $x = 0$ surface. Colors represent the angles between the y and z component of the spin density (see color bar at the bottom); brightness corresponds to magnitude $\|\mathbf{P}\|$. The Weyl points with energies between -65 and -45 meV are color coded as in Fig. 2. When increasing the Fermi energy from (a) to (b) the two Fermi arcs touch and the spin polarization winds around the touching point. A further increase leads to avoided crossings (c) and a surface loop, which is detached from the Weyl points. The spin polarization winds around the loop which becomes larger for higher ϵ_F (d), (a) $\epsilon_F = -57$ meV, (b) $\epsilon_F = -56.5$ meV, (c) $\epsilon_F = -55$ meV, (d) $\epsilon_F = -52$ meV.

An early study proposed that such a detached loop reflects the topological invariant associated with a transition between normal and topological insulators via a Weyl-semimetal phase [50]. A different publication [51] attributed the emergence of a loop to a delicate interplay between inter- and intravalley interactions in a four-valley model for Weyl semimetals. Furthermore, contractible loops on the Fermi surface have also been interpreted as track states [52] or as gapped surface states as a result of quadrupole topology in higher order Weyl semimetals [53]. Here we demonstrated the presence of a detached loop in an *ab initio* derived tight-binding model. To verify whether it is related to the latter concept, further calculations are necessary.

VI. CONCLUSION

We have shown that SOC significantly modifies the band structure of $Pb_9Cu(PO_4)_6O$ leading to the presence of 66 Weyl points and developed an algorithm to efficiently identify their positions. Furthermore, we described the corresponding surface states and found that depending on the actual value of the Fermi energy these can show different features. Especially an avoided crossing is possible that influences the spin polarization of surface states and results in a detached loop not connecting any Weyl points.

The very complex and beautiful Weyl physics described here should be observable in $Pb_9Cu(PO_4)_6O_{1-\delta}$ if the material is cooled to a few kelvin so that the Cu sites order in a long-range pattern. Further, an oxygen off stoichiometry ($\delta \neq 0$) or another means of electron or hole doping of the Mott insulator is needed to turn it into a metal. Different δ's then correspond to different Fermi energies in our theoretical calculation.

Let us also briefly discuss the effects of electronic correlations. Without SOC and symmetry breaking, the self-energy of both Cu orbitals crossing the Fermi energy is locally the same. Thus if the momentum dependence of the self-energy

can be neglected, as it is the case, e.g., in dynamical mean-field theory (DMFT) [54], we have exactly the same dispersive (quasiparticle) bands as in DFT, only renormalized (shrunk) by a momentum independent constant.

With spin-orbit coupling, the self-energy can be different for both Kramers pairs. However, the difference will not be huge since the overall bandwidth is a much larger energy scale than the spin-orbit coupling. This implies electronic correlations can quantitatively change the dispersion and the position of the Weyl points to some extent, but qualitatively we expect the same behavior.

The data of our calculations and the code for the detection of Weyl points are openly available at [55] and [56], respectively.

ACKNOWLEDGMENTS

We would like to thank M. Wallerberger and G. Sangiovanni for many fruitful discussions. Further we acknowledge funding through the Austrian Science Fund (FWF) Projects No. I 5398, No. P 36213, SFB Q-M&S (FWF Project ID F86), and Research Unit QUAST by the Deutsche Foschungsgemeinschaft (DFG; Project ID FOR5249) and FWF (Project ID I 5868). L.S. is thankful for the starting funds from Northwest University. Calculations have been done in part on the Vienna Scientific Cluster (VSC).

APPENDIX A: SYMMETRY

For a Weyl point at a TRIM the absolute value of its Chern number can be derived from symmetry arguments as we have done in Sec. III. Here we provide the details of these arguments starting with the case without SOC, where the TR operator can be represented as $\Theta := e^{-i\pi L_y}\mathcal{K}$ [57]. L_y is the y component of orbital angular momentum and $\mathcal{K}$ denotes complex conjugation. In the basis of the spherical harmonics $Y_2^{\pm 1}$ it can thus be expressed as

$$\Theta = \begin{pmatrix} 0 & -1 \\ -1 & 0 \end{pmatrix}\mathcal{K}. \tag{A1}$$

This allows us to directly calculate how the Pauli matrices in Eq. (1) transform under TR. If we choose the basis of $Y_2^{\pm 1}$ for the d_{xz}/d_{yz} orbitals, which is much more practical

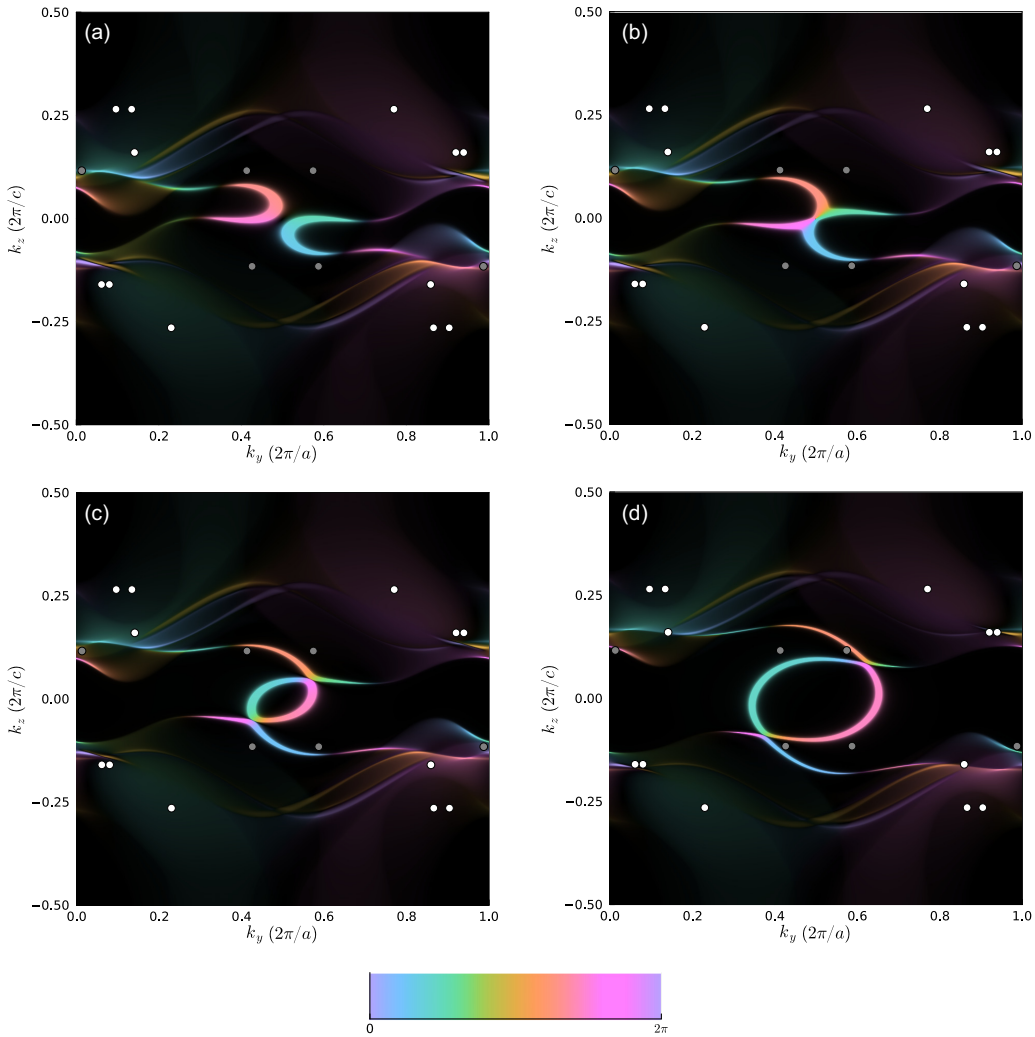

FIG. 5. Same as Fig. 4 but now the colors represent the angles between the x and z component of the spin density. (a) $\epsilon_F = -57$ meV, (b) $\epsilon_F = -56.5$ meV, (c) $\epsilon_F = -55$ meV, (d) $\epsilon_F = -52$ meV.

for the following calculations, $\boldsymbol{\sigma}_x$ and $\boldsymbol{\sigma}_y$ stay invariant and $\boldsymbol{\sigma}_z$ changes sign. Since the Hamiltonian $\mathbf{h}(\mathbf{q}) \cdot \boldsymbol{\sigma}$ must be TR invariant, this implies that the x and y components of $\hat{\mathbf{h}}(\mathbf{q})$ are even functions of $\mathbf{q}$ and $\hat{h}_z(\mathbf{q})$ is odd, i.e.,

$$\hat{\mathbf{h}}(\mathbf{q}) := \begin{pmatrix} \hat{h}_x(\mathbf{q}) \\ \hat{h}_y(\mathbf{q}) \\ \hat{h}_z(\mathbf{q}) \end{pmatrix} = \begin{pmatrix} \hat{h}_x(-\mathbf{q}) \\ \hat{h}_y(-\mathbf{q}) \\ -\hat{h}_z(-\mathbf{q}) \end{pmatrix}. \tag{A2}$$

Now we can deduce the Chern numbers at the TRIM Γ and A using Eq. (3). If we pick a regular value $\boldsymbol{\eta} = \hat{\mathbf{h}}(\mathbf{q}_0)$ at which $\hat{h}_z(\mathbf{q}_0) = 0$, we can conclude from Eq. (A2) that the preimage $\hat{\mathbf{h}}^{-1}(\boldsymbol{\eta})$ contains at least two points $\{\mathbf{q}_0, -\mathbf{q}_0\}$ at which the change in orientation is the same. Hence the degree of $\hat{\mathbf{h}}$ is at least ± 2. In principle every even number would be allowed by symmetry, but one could always introduce a small perturbation that is consistent with symmetry such that the degree would become ± 2. Thus we conclude that the Weyl point's Chern number is ± 2 without SOC. The sign cannot be determined by symmetry only.

For spin-full bands, i.e., with SOC, the situation is different, as the TR operator can be expressed as $\Theta = e^{-i\pi J_y}\mathcal{K}$ with total angular momentum J_y, which has half-integer eigenvalues as opposed to L_y. On the basis of the $(j = \frac{5}{2}, j_z = \pm\frac{1}{2})$ orbitals this takes the form

$$\Theta = \begin{pmatrix} 0 & -1 \\ 1 & 0 \end{pmatrix}\mathcal{K} \tag{A3}$$

and up to an overall minus sign this is the same for the $(j = \frac{5}{2}, j_z = \pm\frac{3}{2})$ orbitals. Again, we can use this to determine how the Pauli matrices transform under TR. Now all of them change sign, which implies that every component of $\hat{\mathbf{h}}(\mathbf{q})$ is an odd function of momentum $\mathbf{q}$.

If there is only the trivial point group present at a Weyl point as it is the case for the TRIM L and M, then the most generic Chern number is ± 1, because without any symmetries the preimage $\hat{\mathbf{h}}^{-1}(\boldsymbol{\eta})$ in Eq. (3) of any regular value $\boldsymbol{\eta}$ generically contains a single point, i.e., symmetry does not enforce $\hat{\mathbf{h}}$ to have the same value at multiple points. However, at Γ and A the point group symmetry can give additional constraints on $\hat{\mathbf{h}}$ depending on the representation of the orbitals.

Under a threefold rotation around the z axis the orbitals acquire phases of $\exp(-\frac{2\pi i}{3} j_z)$. From these we can conclude how the Pauli matrices in Eq. (1) transform: $\sigma_z = |+ j_z\rangle\langle + j_z| - |- j_z\rangle\langle - j_z|$ remains invariant as it does not mix orbitals with opposite j_z. The matrices $\sigma_\pm := (\sigma_x \pm i\sigma_y)/2 = |\pm j_z\rangle\langle \mp j_z|$ mix orbitals with opposite j_z and thus acquire phases of $\exp(\mp 2 \cdot \frac{2\pi i}{3} j_z)$.

In the case of the $j_z = \frac{3}{2}$ bands this phase is just unity, such that $\sigma_\pm$ and consequently also σ_x and σ_y are invariant under the threefold rotation. As the Hamiltonian in Eq. (1) must be invariant, $\mathbf{h}$ must transform dual to the Pauli matrices, which in this case means it stays invariant as well. Thus there are always three points related by the threefold rotation which are mapped onto the same value under $\hat{\mathbf{h}}$. At these points the change of orientation is the same, since rotations preserve orientation. Consequently, Eq. (3) implies Chern numbers equal to plus or minus three for the $j_z = \pm\frac{3}{2}$ bands.

In the case of the $j_z = \frac{1}{2}$ bands the $\sigma_\pm$ matrices acquire a phase of $\exp(\mp\frac{2\pi i}{3})$ such that $(\sigma_x, \sigma_y, \sigma_z)$ transforms as a 3D vector. Again the Hamiltonian in Eq. (1) must be invariant under the threefold rotation and therefore $\mathbf{h}$ must transform as a (dual) vector. However, this implies that a rotation changes the value of $\hat{\mathbf{h}}$ and so for any value there is generically only a single point mapped onto this value. Consequently, the sum in Eq. (3) runs over a single point and therefore the absolute value of the corresponding Chern number is one.

APPENDIX B: SURFACE STATES

The surface spectral spin density $\mathbf{P}(k_y, k_z, \omega = \epsilon_F)$ in Fig. 4 only shows how spin changes in the yz plane when tracing the surface states over the surface Brillouin zone. However, spin is not restricted to this plane. To show this, we present $\mathbf{P}(k_y, k_z, \omega = \epsilon_F)$ in the xz plane (see Fig. 5). We observe the same features as in Fig. 4 from which we conclude that all three spin components wind around the central detached loop.

[1] S. Lee, J. Kim, S. Im, S. An, Y.-W. Kwon, and K. H. Auh, J. Korean Cryst. Growth Cryst. Technol. **33**, 61 (2023).

[2] S. Lee, J.-H. Kim, and Y.-W. Kwon, arXiv:2307.12008 [cond-mat].

[3] S. Lee, J. Kim, H.-T. Kim, S. Im, S. An, and K. H. Auh, arXiv:2307.12037 [cond-mat].

[4] L. Si and K. Held, Phys. Rev. B **108**, L121110 (2023).

[5] L. Si, M. Wallerberger, A. Smolyanyuk, S. di Cataldo, J. M. Tomczak, and K. Held, J. Phys.: Condens. Matter **36**, 065601 (2023).

[6] D. M. Korotin, D. Y. Novoselov, A. O. Shorikov, V. I. Anisimov, and A. R. Oganov, Phys. Rev. B **108**, L241111 (2023).

[7] C. Yue, V. Christiansson, and P. Werner, arXiv:2308.04976 [cond-mat].

[8] J. Liu, T. Yu, J. Li, J. Wang, J. Lai, Y. Sun, X.-Q. Chen, and P. Liu, Phys. Rev. B **108**, L161101 (2023).

[9] A. B. Georgescu, arXiv:2308.07295 [cond-mat].

[10] K. Kumar, N. K. Karn, Y. Kumar, and V. P. S. Awana, ACS Omega **8**, 41737 (2023).

[11] P. Puphal, M. Y. P. Akbar, M. Hepting, E. Goering, M. Isobe, A. A. Nugroho, and B. Keimer, APL Materials **11**, 101128 (2023).

[12] Y. Jiang, S. B. Lee, J. Herzog-Arbeitman, J. Yu, X. Feng, H. Hu, D. Călugăru, P. S. Brodale, E. L. Gormley, M. G. Vergniory, C. Felser, S. Blanco-Canosa, C. H. Hendon, L. M. Schoop, and B. A. Bernevig, arXiv:2308.05143 [cond-mat].

[13] C. Liu, W. Cheng, X. Zhang, J. Xu, J. Li, Q. Shi, C. Yuan, L. Xu, H. Zhou, S. Zhu, J. Sun, W. Wu, J. Luo, K. Jin, and Y. Li, Phys. Rev. Mater. **7**, 084804 (2023).

[14] P. Wang, X. Liu, J. Ge, C. Ji, H. Ji, Y. Liu, Y. Ai, G. Ma, S. Qi, and J. Wang, Quantum Front. **2**, 10 (2023).

[15] S. Zhu, W. Wu, Z. Li, and J. Luo, Matter **6**, 4401 (2023).

[16] P. K. Jain, J. Phys. Chem. C **127**, 18253 (2023).

[17] S. M. Griffin, arXiv:2307.16892 [cond-mat].

[18] J. Lai, J. Li, P. Liu, Y. Sun, and X.-Q. Chen, J. Mater. Sci. Technol. **171**, 66 (2024).

[19] J. Cabezas-Escares, N. F. Barrera, R. H. Lavroff, A. N. A. C. Cardenas, and F. Munoz, arXiv:2308.01135 [cond-mat].

[20] B. T. Zhou and M. Franz, arXiv:2308.07408 [cond-mat].

[21] M. M. Hirschmann and J. Mitscherling, arXiv:2308.03751 [cond-mat].

[22] S. Yang, G. Liu, and Y. Zhong, arXiv:2308.13938 [cond-mat].

[23] K. Koepernik and H. Eschrig, Phys. Rev. B **59**, 1743 (1999).

[24] J. P. Perdew and Y. Wang, Phys. Rev. B **45**, 13244 (1992).

[25] M. Bauernfeind, J. Erhardt, P. Eck, P. K. Thakur, J. Gabel, T.-L. Lee, J. Schäfer, S. Moser, D. Di Sante, R. Claessen, and G. Sangiovanni, Nat. Commun. **12**, 5396 (2021).

[26] P. Eck, C. Ortix, A. Consiglio, J. Erhardt, M. Bauernfeind, S. Moser, R. Claessen, D. Di Sante, and G. Sangiovanni, Phys. Rev. B **106**, 195143 (2022).

[27] W. Fulton and J. Harris, *Representation Theory: A First Course*, Graduate Texts in Mathematics (Springer, New York, 2013).

[28] G. E. Volovik, JETP Lett. **46**, 81 (1987).

[29] V. Palamodov, *Reconstructive Integral Geometry* (Birkhäuser, Boston, 2012).

[30] S. S. Tsirkin, I. Souza, and D. Vanderbilt, Phys. Rev. B **96**, 045102 (2017).

[31] G. Chang, B. J. Wieder, F. Schindler, D. S. Sanchez, I. Belopolski, S.-M. Huang, B. Singh, D. Wu, T.-R. Chang, T. Neupert, S.-Y. Xu, H. Lin, and M. Z. Hasan, Nat. Mater. **17**, 978 (2018).

[32] The little group of a point **k** is also the stabilizer of **k** and is defined by all symmetry operations of the system that leave **k** invariant. The little group being trivial means only the neutral element leaves this point invariant.

[33] H. B. Nielsen and M. Ninomiya, Nucl. Phys. B **185**, 20 (1981).

[34] H. B. Nielsen and M. Ninomiya, Nucl. Phys. B **193**, 173 (1981).

[35] Q. Xu, Y. Zhang, K. Koepernik, W. Shi, J. van den Brink, C. Felser, and Y. Sun, npj Comput. Mater. **6**, 32 (2020).

[36] H. Saini, M. Laurien, P. Blaha, and O. Rubel, Comput. Phys. Commun. **270**, 108147 (2022).

[37] Q. Wu, S. Zhang, H.-F. Song, M. Troyer, and A. A. Soluyanov, Comput. Phys. Commun. **224**, 405 (2018).

[38] M. V. Berry, Proc. R. Soc. London, A **392**, 45 (1997).

[39] M. Fecko, *Differential Geometry and Lie Groups for Physicists* (Cambridge University Press, Cambridge, UK, 2006).

[40] C. Rackauckas and Q. Nie, J. Open Res. Softw. **5**, 15 (2017).

[41] E. Anderson, Z. Bai, C. Bischof, S. Blackford, J. Demmel, J. Dongarra, J. Du Croz, A. Greenbaum, S. Hammarling, A. McKenney, and D. Sorensen, *LAPACK Users' Guide*, 3rd ed. (Society for Industrial and Applied Mathematics, Philadelphia, PA, 1999).

[42] H. Weng, C. Fang, Z. Fang, B. A. Bernevig, and X. Dai, Phys. Rev. X **5**, 011029 (2015).

[43] X. Wan, A. M. Turner, A. Vishwanath, and S. Y. Savrasov, Phys. Rev. B **83**, 205101 (2011).

[44] I. Belopolski, S.-Y. Xu, D. S. Sanchez, G. Chang, C. Guo, M. Neupane, H. Zheng, C.-C. Lee, S.-M. Huang, G. Bian, N. Alidoust, T.-R. Chang, B. K. Wang, X. Zhang, A. Bansil, H.-T. Jeng, H. Lin, S. Jia, and M. Z. Hasan, Phys. Rev. Lett. **116**, 066802 (2016).

[45] N. P. Armitage, E. J. Mele, and A. Vishwanath, Rev. Mod. Phys. **90**, 015001 (2018).

[46] A. Damascelli, Z. Hussain, and Z.-X. Shen, Rev. Mod. Phys. **75**, 473 (2003).

[47] F. D. M. Haldane, arXiv:1401.0529 [cond-mat].

[48] M. Hoesch, T. Greber, V. N. Petrov, M. Muntwiler, M. Hengsberger, W. Auwärter, and J. Osterwalder, J. Electron Spectrosc. Relat. Phenom. **124**, 263 (2002).

[49] B. Lv, T. Qian, and H. Ding, Nat. Rev. Phys. **1**, 609 (2019).

[50] S.-M. Huang, S.-Y. Xu, I. Belopolski, C.-C. Lee, G. Chang, B. Wang, N. Alidoust, G. Bian, M. Neupane, C. Zhang, S. Jia, A. Bansil, H. Lin, and M. Z. Hasan, Nat. Commun. **6**, 7373 (2015).

[51] Z. A. Devizorova and V. A. Volkov, Phys. Rev. B **95**, 081302(R) (2017).

[52] T. M. McCormick, I. Kimchi, and N. Trivedi, Phys. Rev. B **95**, 075133 (2017).

[53] H.-X. Wang, Z.-K. Lin, B. Jiang, G.-Y. Guo, and J.-H. Jiang, Phys. Rev. Lett. **125**, 146401 (2020).

[54] A. Georges, G. Kotliar, W. Krauth, and M. J. Rozenberg, Rev. Mod. Phys. **68**, 13 (1996).

[55] https://nomad-lab.eu/prod/v1/staging/gui/user/uploads/upload/id/LM9OlhazTwu7LhSMEjF9WQ.

[56] https://github.com/martinbrass/TightBindingToolBox.git.

[57] I. I. Geru, I. I. Geru, and Evenson, *Time-Reversal Symmetry* (Springer, Berlin, 2018).